OPEN

NPG Asia Materials (2016) 8, e313; doi:10.1038/am.2016.146
www.nature.com/am

ORIGINAL ARTICLE

Magnetic nanoparticle-promoted droplet vaporization for *in vivo* stimuli-responsive cancer theranostics

Yang Zhou[1,2,7], Ronghui Wang[3,7], Zhaogang Teng[4], Zhigang Wang[3], Bing Hu[1], Michael Kolios[5], Hangrong Chen[6], Nan Zhang[3], Yanjie Wang[5], Pan Li[3], Xing Wu[1], Guangming Lu[4], Yu Chen[6] and Yuanyi Zheng[1,3]

The development of efficient strategies for *in vivo* stimuli-responsive cancer treatment and personalized biomedicine is a great challenge. To overcome the critical issues and limitations of traditional protocols using acoustic droplet vaporization and optical droplet vaporization in stimuli-responsive tumor treatment, we herein report a new strategy, magnetic droplet vaporization (MDV), based on nanobiotechnology, for efficient magnetic field-responsive cancer theranostics. Perfluorohexane (PFH)-encapsulated superparamagnetic hollow iron oxide nanoparticles with a high magnetic-thermal energy transfer capability quickly respond to an external alternating current (a.c.) magnetic field to produce thermal energy and raise the temperature of the surrounding tumor tissue. The encapsulated PFH, with a desirable boiling point of ~ 56 °C, can be vaporized to enhance the performance of ultrasound imaging of tumors, as systematically demonstrated both *in vitro* and *in vivo*. The magnetic–thermal energy transfer further ablated and removed tumors in mice tumor xenograft models. This unique MDV principle with high versatility and performance is expected to broaden the biomedical applications of nanotechnology and promote clinical translations of intelligent diagnostic and therapeutic modalities, especially for battling cancer.
NPG Asia Materials (2016) **8,** e313; doi:10.1038/am.2016.146; published online 23 September 2016

INTRODUCTION

The rapid progress of nanotechnology in biomedicine provides an alternative highly versatile and efficient methodology for improving the sensitivity, resolution and precision of various diagnostic imaging modalities and enhancing the therapeutic efficiency of diverse treatment protocols, especially for the early detection and efficient killing of cancer cells.[1–6] The concept of molecular imaging and synergistic therapy based on nanoparticles (NPs) as the contrast agents (CAs) or synergistic agents (SAs) possesses promising clinical applications to benefit human health due to their high biocompatibility and biomedical performance.[7–11] Compared with other imaging modalities, such as magnetic resonance imaging, computed tomography and radionuclide imaging, ultrasound-based molecular imaging develops more slowly because of its intrinsic imaging bottleneck, that is, the particle size of CAs (for example, microbubbles) for ultrasonography must be large enough to effectively respond to the ultrasound waves.[12–14] Such CAs with large particulate sizes are more easily taken up by the reticuloendothelial system, severely restricting their accumulation in tumors and subsequent molecular imaging functions for early tumor detection.[13,14] In addition, the development of SAs for ultrasound-based synergistic therapy (for example, high-intensity focused ultrasound) also encounters a similar particle size issue compared with other SA-based synergistic therapies such as radiosensitization and/or chemotherapy.[15]

It remains a great challenge to solve the critical particle size issue for ultrasound-based molecular imaging and therapy. Phase-changing nanoprobes with unique stimuli-responsive behaviors are one of the most effective CAs and SAs for ultrasonography and ultrasound therapy. These nanoprobes circulate within blood vessels and penetrate tumor tissues when they are in the form of nano-sized particles.[13,16,17] Upon external triggering, these nano-sized CAs or SAs can evaporate to generate large micrometer-sized bubbles and substantially enhance the ultrasonography and therapeutic

[1]Shanghai Institute of Ultrasound in Medicine, Shanghai Jiaotong University Affiliated Shanghai Sixth People's Hospital, Shanghai, China; [2]Third People's Hospital of Chengdu, Chengdu, China; [3]Second Affiliated Hospital of Chongqing Medical University, Chongqing, China; [4]Department of Medical Imaging, Jinling Hospital, School of Medicine, Nanjing University, Nanjing, China; [5]Department of Physics, Ryerson University, Toronto, Ontario, Canada and [6]State Key Laboratory of High Performance Ceramics and Superfine Microstructure, Shanghai Institute of Ceramics, Chinese Academy of Sciences, Shanghai, China
[7]These authors contributed equally to this work.
Correspondence: Professor G Lu, Department of Medical Imaging, Jinling Hospital, School of Medicine, Nanjing University, 305 Zhongshan Dong Road, Nanjing 210002, China.
E-mail: cjr.luguangming@vip.163.com
or Professor Y Chen, State Key Laboratory of High Performance Ceramics and Superfine Microstructure, Shanghai Institute of Ceramics, Chinese Academy of Sciences, 1295 Dingxi Road, Shanghai 200050, China.
E-mail: chenyu@mail.sic.ac.cn
or Professor Y Zheng, Shanghai Institute of Ultrasound in Medicine, Shanghai Jiaotong University Affiliated Shanghai Sixth People's Hospital, 600 Yishan Road, Shanghai 200233, China.
E-mail: zhengyuanyi@gmail.com
Received 27 February 2016; revised 29 June 2016; accepted 12 July 2016

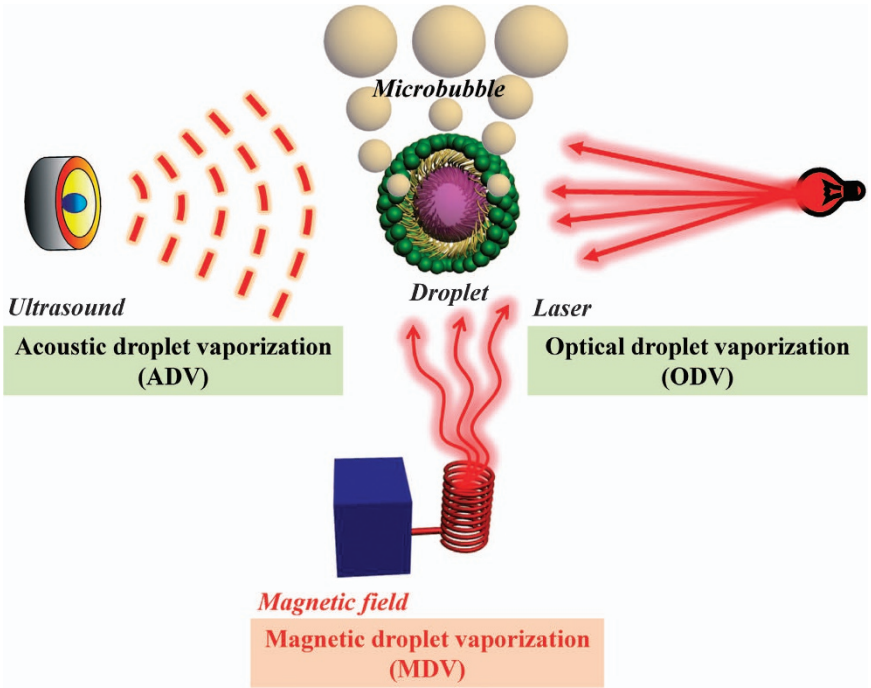

Figure 1 The scheme of acoustic droplet vaporization (ADV), optical droplet vaporization (ODV) and magnetic droplet vaporization (MDV) processes. Schematic illustration of three representative vaporization principles for intelligent stimuli-responsive phase transformation to enhance the performance and efficiency of ultrasound-based diagnostic imaging and therapy. These three modalities include ADV, ODV and MDV using ultrasound, laser and magnetic field as the external triggers, respectively.

performance. Two approaches have been developed to achieve this specific phase transformation process (Figure 1). One is acoustic droplet vaporization (ADV) and the other is optical droplet vaporization (ODV). Typically, ADV employs acoustic waves to evaporate the liquid droplets.[18–20] However, because ultrasound is easily and substantially influenced by gas or bone, the use of ADV is restricted in vascular imaging, cancer detection and drug delivery. ODV uses a laser as the excitation source to induce the vaporization of liquid droplets. Biocompatible metal NPs are generally employed to convert photons into thermal energy and induce the evaporation of liquid droplets.[21–23] The shallow penetration depth of the laser, however, substantially hinders its further clinical translation. It is noted that both ADV and ODV require a pre-determined tumor position to accomplish site-specific phase transformation for imaging and therapy, which means that these two modalities cannot intrinsically overcome the drawbacks of particle sizes of CAs or SAs for early diagnosis and efficient therapy of cancer.

MATERIALS AND METHODS

Synthesis of HIONs- and PFH-loaded HIONs (PFH-HIONs)

Synthesis of HIONs. Superparamagnetic hollow iron oxide nanoparticles (HIONs) were synthesized by a one-pot solvothermal process. $FeCl_3{\cdot}6H_2O$ (1.350 g, Sinopharm Chemical Reagent, Shanghai, China) was initially dissolved in ethylene glycol (Sinopharm Chemical Reagent) by magnetic stirring followed by adding ammonium acetate (NH_4Ac, 3.854 g, Sinopharm Chemical Reagent) into the solution. After further stirring at room temperature for 3 h, 100 ml of solution was transferred into a Teflon-lined stainless steel autoclave. The autoclave was incubated in an oven at 200 °C for 24 h. After cooling the autoclave to room temperature, the black precipitate was collected by a magnet and washed several times with water and ethanol. The final product was freeze-dried for further use.

Synthesis of PFH-HIONs. To encapsulate perfluorohexane (PFH) (Sigma-Aldrich, Shanghai, China) into HIONs, HION powder from lyophilization (5, 10, 20 or 40 mg) was vacuum sealed in 2 ml vials, and then PFH (0.5 ml) was injected into each vial to ensure that the powder was immersed in PFH. Last, the vials were kept at 4 °C for 24 h, after which the PFH-HIONs were harvested after extraction of excess PFH. Finally, PFH was encapsulated within the hollow interior by adding saline to seal it within HIONs. HIONs without PFH encapsulation were prepared by replacing PFH with degassed water in the above procedure.

In vivo magnetic hyperthermia efficacy and phase transformation

Animal tumor xenograft. The human breast cancer cell line MDA-MB-231 (ATCC Cat. No. HTB-26) was cultured in DMEM medium (Invitrogen Corporation, Carlsbad, CA, USA) with 10% fetal bovine serum. About 0.2 ml of serum-free DMEM-diluted MDA-MB-231 cell suspension (1×10^6 cells per ml) was directly injected into the flanks of 4-week-old female Balb C nu/nu mice, which were further housed and fed in constant temperature and humidity conditions. Approximately 2–3 weeks later, the nude mice with tumor volumes of 0.8–1 cm^3 were picked out randomly to undergo *in vivo* experiments. All animal experiments were performed in accordance with the guidelines of the Institutional Animal Care and Use Committee of the University.

In vivo magnetic hyperthermia. Nude mice bearing MDA-MB-231 xenograft tumors received intra-tumor administration of PFH-HIONs (0.3 ml, 40 mg ml^{-1}), HIONs (0.3 ml, 40 mg ml^{-1}) or saline solution after intraperitoneal anesthesia with pentobarbital sodium. The mice were randomly divided into three groups ($n = 10$ in each group) using the 'simple randomization' method after the tumor model establishment. The liquids were precisely injected into the center of tumors under the guidance of ultrasonography for localized cancer imaging and therapy. Then, the mice were transferred to the center of an electromagnetic induction heating coil of a homemade magnetic hyperthermia analyzer where tumors were paralleled the coil plane and separated from the coil. The thermal images were recorded by a far Infrared imager (Fluke, Ti32, Everett, WA, USA) every 10 s. The

temperatures of the tumor were analyzed on the thermal images by SmartView 3.3 software (Smart Digital Networks, Inc, Los Angeles, CA, USA). The magnetic irradiation stopped after 3 min. Half of the mice were killed 24 h after treatment for pathological study. The remaining mice were fed for further observations and tumor monitoring. The tumor volume of mice was measured every 2 days after the magnetic hyperthermia. The tumor volumes were calculated according to the following formula: $V = (W^2 \times L)/2$ (L: the longest size of the tumor, W: the shortest diameter, perpendicular to length). The a.c. magnetic field of 626 kHz at 6 kW was adopted for magnetic hyperthermia treatment of the tumors. If a mouse died within 14 days after treatment, it was excluded from the analysis. An open trial method was employed in this study.

TTC stain. The tumors after magnetic hyperthermia were anatomized, cut from the middle and put into TTC solution (2% W/V, Sigma-Aldrich, St Louis, MO, USA). Approximately 10 min later, the specimens were taken out to observe the therapeutic efficacy of magnetic hyperthermia.

In vivo observation of the MDV process after the injection of PFH-HIONs. *In vivo* ultrasonography was carried out *in situ* to observe the phase transformation of PFH-HIONs after exposure to the a.c. magnetic field. The imaging modes (B-mode and CEUS mode) and parameters were the same as *in vitro* ultrasonography, as described in the Supplementary Information.

Pathology of tumors after MDV and magnetic hyperthermia. To reveal the molecular mechanism of magnetic hyperthermia, the pathological analysis, including hematoxylin and eosin staining (H&E) staining, and immunohistochemistry analysis of the tumor proliferation and necrosis (TUNEL, proliferating cell nuclear antigen (PCNA), BCL-2, and Baxand caspases) were conducted on the anatomized tumor slices according to standard procedures. H&E staining and Prussian blue staining of the main organs were conducted after the therapeutic process followed by another 2 weeks of feeding. In addition, the serum biochemical levels of TP, ALB, ALT, AST, BUN and sCr of mice were assessed at the end of therapy.

RESULTS AND DISCUSSION

Design of MDV strategy for stimuli-responsive cancer theranostics

Non-invasive magnetic heat induction is a new irradiation source to convert radiofrequency electromagnetic waves into thermal energy, and the tissue penetration depth is not limited.[24,25] In an attempt to develop new intelligent responsive strategies to solve the critical issues and limitations of ADV and ODV, we propose and design a new liquid–gas phase-transformation strategy, that is, magnetic droplet vaporization (designated as MDV), for efficient magnetic field-responsive cancer theranostics. This MDV process employs an external alternating current (a.c.) magnetic field to generate thermal energy mediated by magnetic NPs, which can subsequently induce the vaporization of encapsulated biocompatible liquid droplets with low boiling points (b.p.). Systematic *in vitro* and *in vivo* investigations have been conducted to successfully demonstrate the feasibility and efficiency of MDV for cancer theranostics. Compared with ODV, MDV adopts magnetic field as the triggering source, which has higher tissue penetration capability compared with the light used as the irradiation source for ODV. In addition, MDV cannot be influenced by gas or bone, which often occurs during the ADV process.

The following two crucial factors determine the feasibility and efficiency of the MDV process: magnetic NPs and liquid droplets. The magnetic NPs should possess a high thermal-energy transfer capability, whereas the liquid droplets should have an adequate b.p. to respond quickly to the introduced thermal energy. In addition, the liquid droplets should be perfectly integrated into magnetic NPs to realize the MDV process. Building on our previous work that perfluorocarbon (PFC) could be encapsulated into hollow mesoporous silica,[26] PLGA capsules[27] or micelles,[16] we herein design and fabricate superparamagnetic porous HIONs as the carriers for the encapsulation and delivery of the hydrophobic PFC droplets. The physicochemical properties of PFC also substantially determine the MDV process

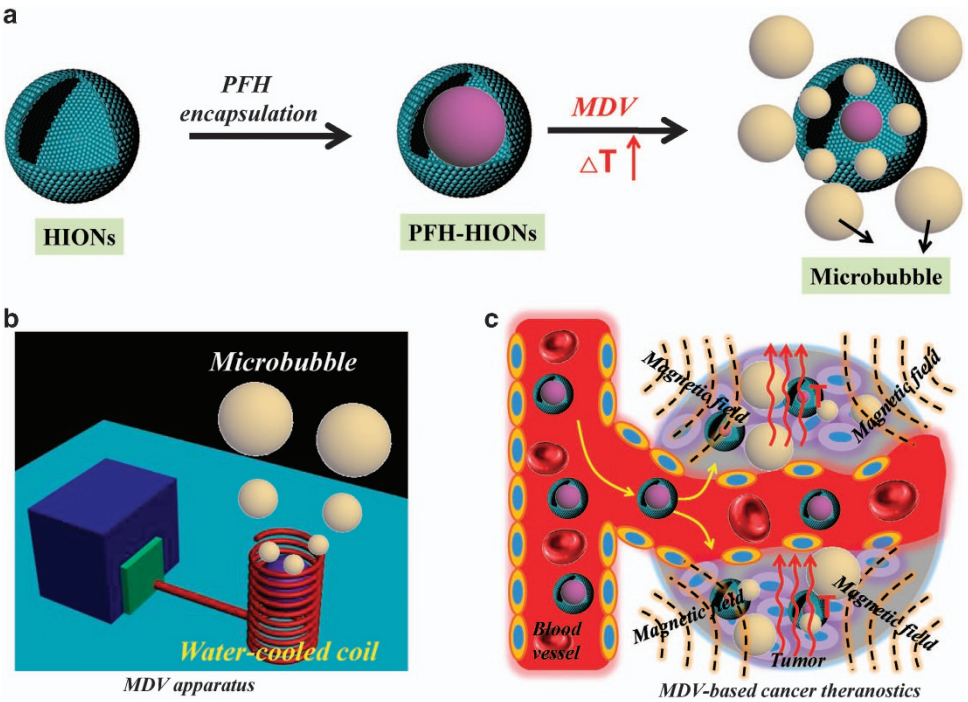

Figure 2 Design of perfluorohexane (PFH)-loaded magnetic hollow iron oxide nanoparticles (HIONs) for magnetic droplet vaporization (MDV)-based intelligent stimuli-responsive cancer theranostics. (**a**) Schematic illustration of the MDV process mediated by PFH-HIONs, including encapsulation of PFH into HIONs and subsequent vaporization of PFH induced by the a.c. magnetic field. (**b**) The scheme of the MDV apparatus for MDV process to generate microbubbles. (**c**) *In vivo* MDV process for imaging-guided cancer theranostics.

and hence the resulting theranostic effects on cancer where the biocompatibility and b.p. have the significant role. As shown in Figure 2a, biocompatible PFH with a b.p. of ~56 °C was initially chosen for encapsulation in the large hollow interior of HIONs (PFH-HIONs), followed by PFH vaporization upon the exposure of PFH-HIONs to a.c. magnetic field (Figure 2b). PFH was chosen over other PFCs for several reasons. The most adopted PFC is perfluoropentane (PFP), with a b.p. of 29 °C. The b.p. increases to ~30–37 °C, depending on the surfactants used to encapsulate PFP.[28,29] Despite the increase in b.p., PFP droplets have to be prepared in an ice-cold water bath and they are unstable in −4 °C storage, making handling and control difficult for their irreversible droplet-to-bubble transition upon injection. Other biocompatible PFCs, such as perfluorohexyl bromide (PFHB), perfluorooctyl bromide (PFOB) and perfluoro-15-crown-5-ether (PFCE), have high b.p. of 97 °C, 142 °C and 146 °C, respectively (Supplementary Table S1), which are too high to be vaporized quickly.

PFH-HIONs can enter the tumor tissues because their small particle sizes are less than the limitation of the specific large pores of capillaries (<700 nm) in the leaky vasculature of the tumor (Figure 2c).[30] They can substantially enhance the ultrasonography performance once the MDV process is initiated because of the production of large numbers of microbubbles. The MDV process can simultaneously generate the thermal energy to ablate and remove the tumor tissues. Importantly, the superparamagnetic HIONs can concurrently act as the CAs for T_2-weighted magnetic resonance imaging. Thus, the MDV process assisted by PFH-HIONs can exert the unique function for imaging-guided hyperthermia of cancer.

Synthesis and characterization of PFH-loaded HIONs

Porous superparamagnetic HIONs were synthesized by a simple but highly versatile one-pot solvothermal synthesis.[31] Iron (III) chloride hexahydrate ($FeCl_3{\cdot}6H_2O$) was employed as the precursor for the synthesis, which was reduced by ethylene glycol (also as the solvent) under solvothermal condition (200 °C) for 24 h. Ammonium acetate was added during the synthesis to avoid aggregation and guarantee high dispersity of as-synthesized HIONs. The formation of the hollow nanostructure of HIONs was based on the principle of Ostwald ripening during the solvothermal process at high temperature and pressure. As shown in Figure 3a–c and Supplementary Figure S1, the fabricated HIONs show a well-defined spherical morphology with the average particle size of 537.3 nm as determined by transmission electron microscopy (615.1 nm as determined by dynamic light scattering, Supplementary Figure S2). The contrast difference between the core and shell indicates the formation of a hollow structure. To reveal the detail of the hollow structure of HIONs, area (Figure 3d and e) and linear (Figure 3f) element mapping were conducted. The interior of the HIONs exhibited much weaker Fe and O element signal intensities compared with the composition of the shell, further revealing the presence of a hollow structure. The crystallinity of as-synthesized HIONs was demonstrated by X-ray diffraction (Supplementary Figure S3) and Fourier Transform infrared spectroscopy (FTIR; Supplementary Figure S4), which can be indexed to the standard X-ray diffraction pattern (JCPDS 19-0629) and Fe-O stretching vibration mode of Fe_3O_4. The high crystallinity of HIONs guarantees their desirable magnetic properties. The magnetic hysteresis loop of HIONs at 300 K exhibits a typical superparamagnetic feature with a saturation magnetization of 87.8 emu g^{-1} (Supplementary Figure S5). Such a high saturation magnetization endows HIONs with a desirable magnetic thermal transfer efficiency for the MDV process.

In vitro and *in vivo* magnetic field-responsive ultrasound imaging

We first investigated the *in vitro* magnetic–thermal transition efficiency of as-synthesized PFH-loaded HIONs. Hydrophobic PFH was sealed

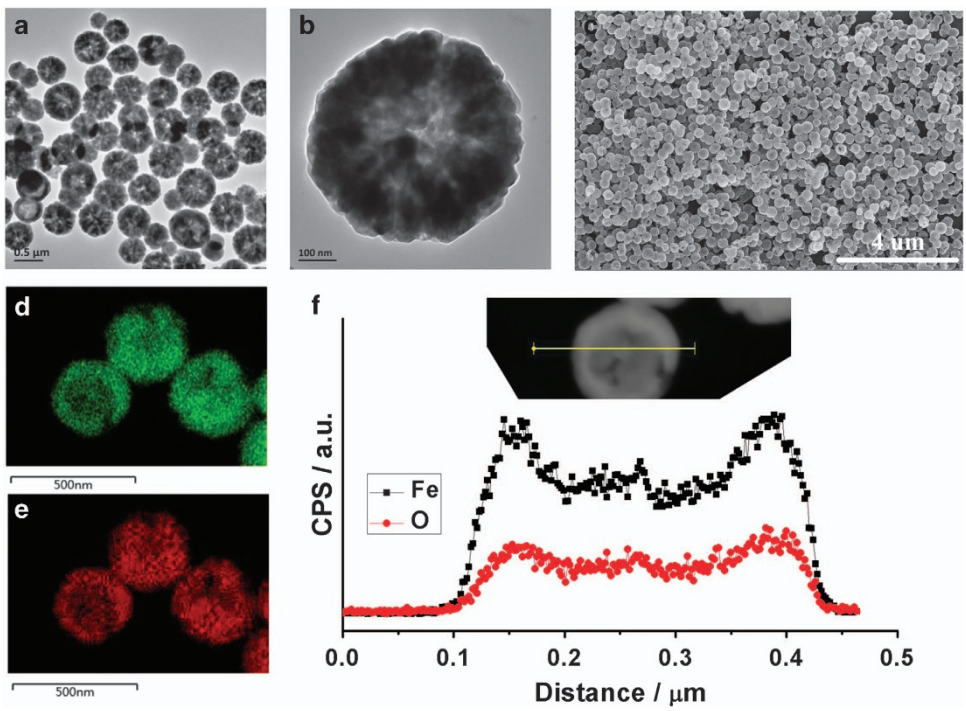

Figure 3 Structural/compositional characterizations of hollow iron oxide nanoparticles (HIONs). Transmission electron microscopy (TEM) images of HIONs at (**a**) low and (**b**) high magnifications. (**c**) Scanning electron microscope image of HIONs. Element mapping of (**d**) Fe and (**e**) O of HIONs. (**f**) The distribution of Fe and O elements by linear scanning of the inset dark-field TEM image.

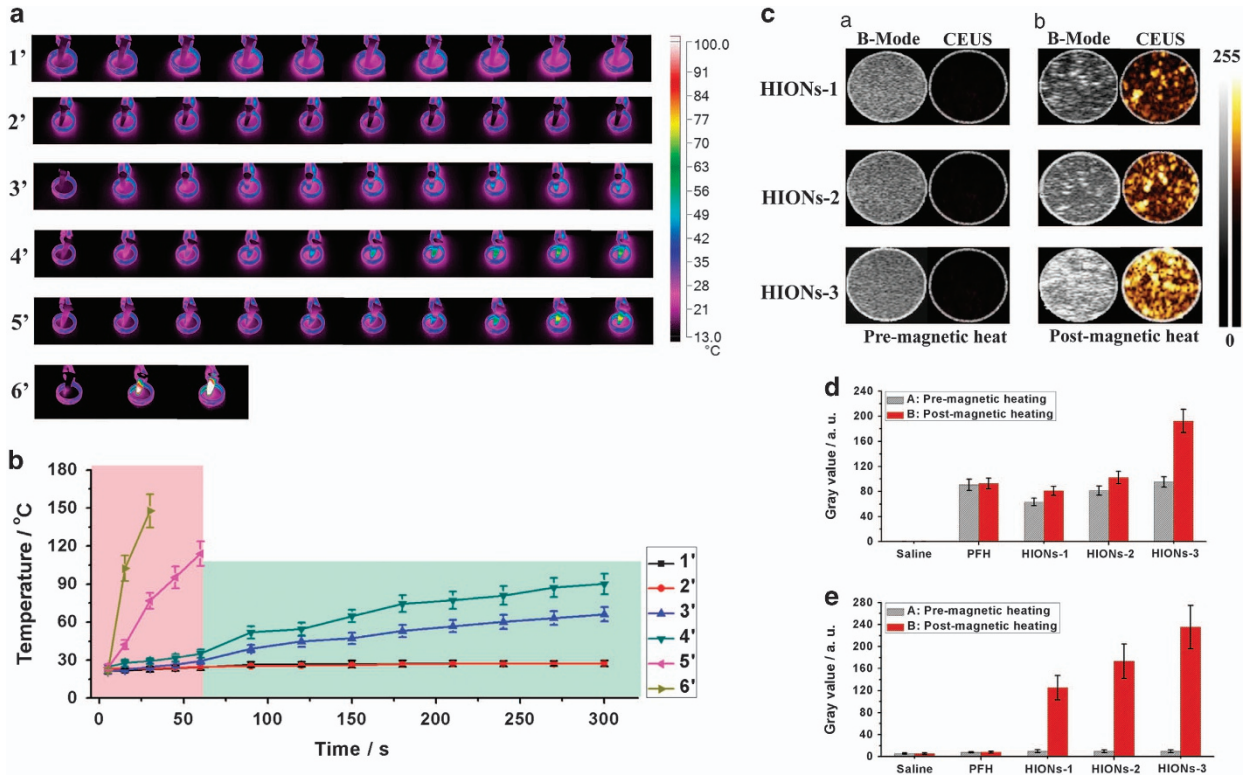

Figure 4 *In vitro* magnetothermal performance of perfluorohexane-hollow iron oxide nanoparticles (PFH-HIONs) and the corresponding magnetic droplet vaporization (MDV) process for contrast-enhanced ultrasound imaging. (**a**) *In vitro* magnetic thermal images of saline (1′), PFH (2′) and PFH-HIONs at different concentrations (3′: 5 mg ml^{-1}, 4′: 10 mg ml^{-1}, 5′: 20 mg ml^{-1} and 6′: 40 mg ml^{-1}). The images of 1′, 2′, 3′ and 4′were taken every 30 s, and the images of 5′ were acquired every 15 s. The images in 6′ were recorded at 5, 15 and 30 s after the heating by a.c. magnetic field. (**b**) Quantitative temperature curve of saline, PFH and PFH-HIONs at different concentrations after the exposure to the a.c. magnetic field for prolonged durations. (**c**) *In vitro* ultrasound imaging of PFH-loaded HIONs at different HION concentrations (HIONs: 30 mg ml^{-1}, PFH-HIONs-1: 10 mg ml^{-1}, PFH-HIONs-2: 20 mg ml^{-1} and PFH-HIONs-3: 30 mg ml^{-1}) and different ultrasonography modes (B-mode and CEUS mode) before (**a**) and after (**b**) the magnetic heating. (**d**: B-mode, **e**: CEUS mode) Quantitative gray values of ultrasound images corresponding to images of (**c**) and Supplementary Figure S8.

in the hollow interior of HIONs by a vacuum-assisted impregnation process.[32] Magnetic heating behavior (Figure 4a) could be observed by dispersing HIONs into aqueous solution followed by exposure to a.c. magnetic field. The temperature of the aqueous solution increased quickly by this magnetic–thermal process. The temperature increased to 66.2 ± 5.7 and 90.1 ± 8.1 °C at an HION concentration of 5 and 10 mg ml^{-1}, respectively, after exposure to the a.c. magnetic field for 5 min (Figure 4b). The quick increase in temperature strongly depends on the HION concentration. HIONs at a concentration of 20 or 40 mg ml^{-1} caused the temperature to increase to 76.7 ± 6.4 or 147.8 ± 13.2 °C, respectively, after the exposure to the a.c. magnetic field for only 30 s. In comparison, a low concentration of PFH-HIONs did not easily increase the temperature of aqueous solutions (Supplementary Figure S6).

Such a high magnetic-thermal transfer efficiency is expected to easily induce the MDV process. To validate this idea, PFH with a b.p. of ~56 °C was encapsulated into HIONs for intelligent magnetic field-responsive ultrasound imaging. Large amounts of microbubbles with different diameters could be generated from PFH-HIONs according to optical microscopic images (Supplementary Figure S7) after the magnetic heating of a PFH-HION suspension. The control group of pure HIONs could not produce microbubbles under the same magnetic irradiation conditions. The generation of microbubbles was observed *insitu* by *in vitro* ultrasound imaging. There were no obvious changes in ultrasound signals in the degassed saline and the suspension of HIONs encapsulating saline before and after exposure to the a.c. magnetic field (Supplementary Figure S8). Significantly improved contrast-enhanced ultrasonography was observed in PFH-HION suspensions at the B-mode and the CEUS mode using either magnetic heating (Figure 4c) or direct heating to 65 °C in a water bath (Supplementary Figure S9 and Movie 1). The contrast enhancement of ultrasound imaging under a magnetic field is also concentration-dependent because the presence of more magnetic HIONs facilitates the fast elevation of the temperature and generation of microbubbles (Figure 4d). A significant contrast enhancement in the CEUS mode (Figure 4e) further demonstrates the generation of microbubbles because this contrast-based ultrasound imaging modality only responds to microbubbles compared with other imaging modes, such as the B-mode or the Harmonic mode. In addition to MDV mediated by PFH-HIONs, such an organic–inorganic hybrid nanosystem, can also concurrently realize the ODV (Supplementary Figure S10) and MDV (Supplementary Figure S11) processes, demonstrating their feasibility for multi-purpose cancer theranostics.

The performance of PFH-HIONs for MDV was further evaluated *in vivo* in nude mice bearing MDA-MB-231 breast cancer xenografts. After the intratumoral administration of saline, PFH, HIONs or PFH-HIONs (0.3 ml, 40 mg ml^{-1}), the mice were exposed to the a.c. magnetic field for magnetic–thermal transition and a further MDV procedure. The tumor temperature quickly increased to 99.7 ± 9.8 and 102.3 ± 9.8 °C after magnetic heating of mice with HIONs and

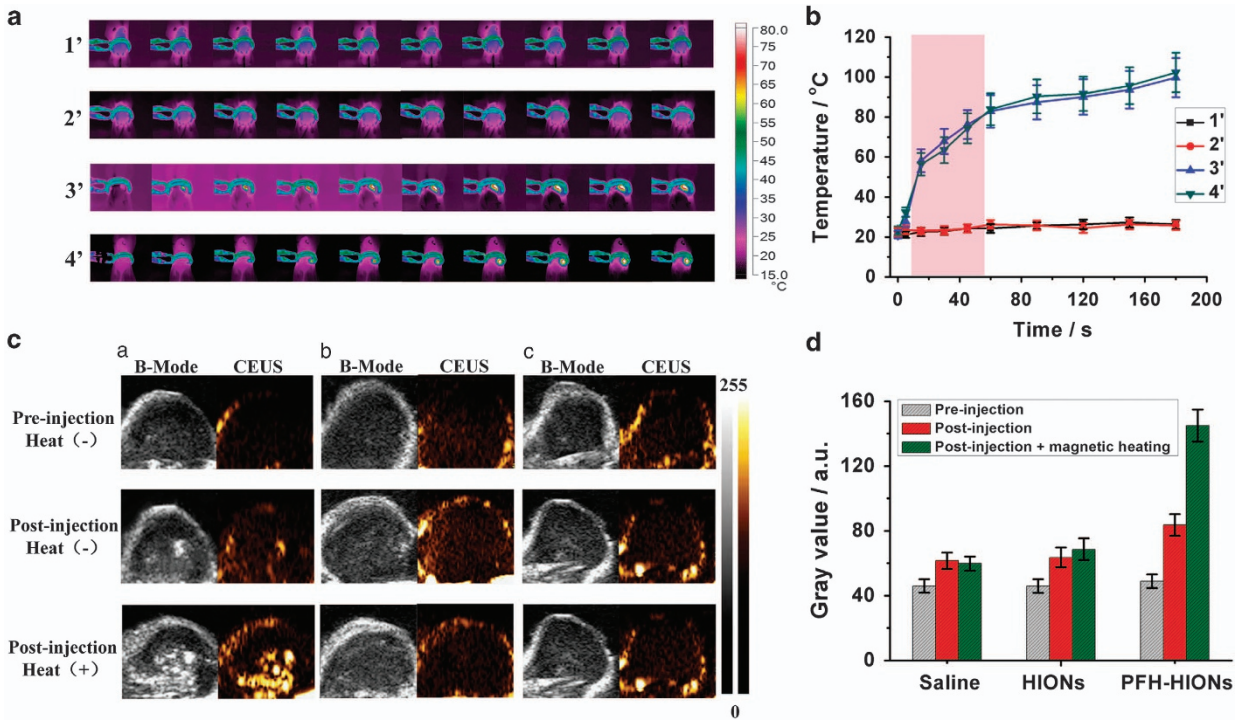

Figure 5 *In vivo* magneto thermal performance of perfluorohexane-hollow iron oxide nanoparticles (PFH-HIONs) and the corresponding magnetic droplet vaporization (MDV) process for contrast-enhanced ultrasound imaging. (**a**) Thermal images of mice after the administration of (1′) saline, (2′) PFH, (3′) HIONs and (4′) PFH-HIONs. (**b**) Quantitative temperature time curve of tumor tissue corresponding to thermal images of (**a**). (**c**) *In vivo* ultrasound imaging of tumors before and after the administration of (a) PFH-HIONs, (b) HIONs and (c) saline, and the subsequent exposure to the a.c. magnetic field. (**d**) *In vivo* quantitative gray values of tumor corresponding to the images of (**c**).

PFH-HIONs, respectively, after only 3 min (Figure 5a and b). The fast temperature elevation vaporized the encapsulated PFH within the hollow interior of HIONs, as demonstrated by the significant contrast enhancement of ultrasound imaging at both the B-mode and CEUS mode (Figure 5c). The quantitative gray values (Figure 5d) further reveal that the ultrasound signal intensity increased 1.7-fold whereas the other two groups had no obvious signal intensity elevation, demonstrating the high *in vivo* MDV efficiency of PFH-HIONs for ultrasonography.

In vivo magnetic hyperthermia of tumors

In addition to MDV for contrast-enhanced intelligent ultrasound imaging, the high magnetic-thermal transfer efficiency of HIONs could be further employed for magnetic ablation of tumors by hyperthermia. The tumor growth was efficiently inhibited within a short time after magnetic hyperthermia assisted by PFH-HIONs (88% inhibition rate within 4 days and 100% inhibition rate within 14 days, Figure 6a–e) compared with the control group. The tumors had disappeared in mice without obvious reoccurrence after the treatment for 2 weeks. Therefore, the MDV process is capable of ultrasound-guided magnetic hyperthermia of cancer.

To further investigate the molecular mechanism of the high *in vivo* magnetic ablation efficiency, tumor pathology after magnetic ablation was systematically investigated. Hematoxylin and eosin (H&E) staining results show an obvious boundary between necrotic and non-necrotic regions in the tumor section after magnetic hyperthermia in the PFH-HIONs group (Figure 6f). The accumulation of PFH-HIONs was also clearly observed in the necrotic region, indicating that the necrotic effect was assisted by PFH-HIONs. Coagulated necrosis was also accompanied by the disappearance of cell structures, fragmentation of lysed cell membranes and ruptured nuclei. In comparison, the structure of tumor tissue and cell membranes were clear and intact and the nuclei were hyperchromatic in the control group.

The PCNA immunohistochemical staining results showed that many proliferating tumor cells with brown nuclei were present in tumor slices in the control group after magnetic ablation (Figure 6g), but few proliferating tumor cells were observed in the PFH-HIONs group, neither in the necrotic region nor the non-necrotic region. The PCNA immunohistochemical staining results are consistent with Bax analysis, where many dead cells with brown color were observed (Supplementary Figure S12). TUNEL staining results showed that many apoptotic tumor cells with brown nuclei were observed in tumor slices in the non-necrotic region of the group that received PFH-HIONs (Figure 6h), indicating that PFH-HION-assisted magnetic hyperthermia could efficiently cause the apoptosis of cancer cells. In Bcl-2 immunohistochemical staining, the apoptosis suppressor gene *Bcl-2* assay showed that significant Bcl-2 expression inside the cell cytoplasm (brown) could be observed in the saline group (Figure 6i), but lower Bcl-2 expression was present in cells in the PFH-HIONs group, in both the necrotic and non-necrotic regions. In caspase immunohistochemical staining, the apoptosis-related cysteine protease caspases assay showed that there was significant caspase expression inside the cell cytoplasm (brown) in the non-necrotic region of tumors that received PFH-HIONs (Figure 6j). Lower caspase expression was observed in the saline group.

The development of intelligent stimuli-responsive cancer treatment modalities is of great significance for personalized biomedicine.[33] The triggers can be intrinsic to the microenvironment, such as enzymes, a lowered pH value or elevated reducing conditions,[34–36] or external such as artificially introduced light, ultrasound or magnetic field.[37–43] Such

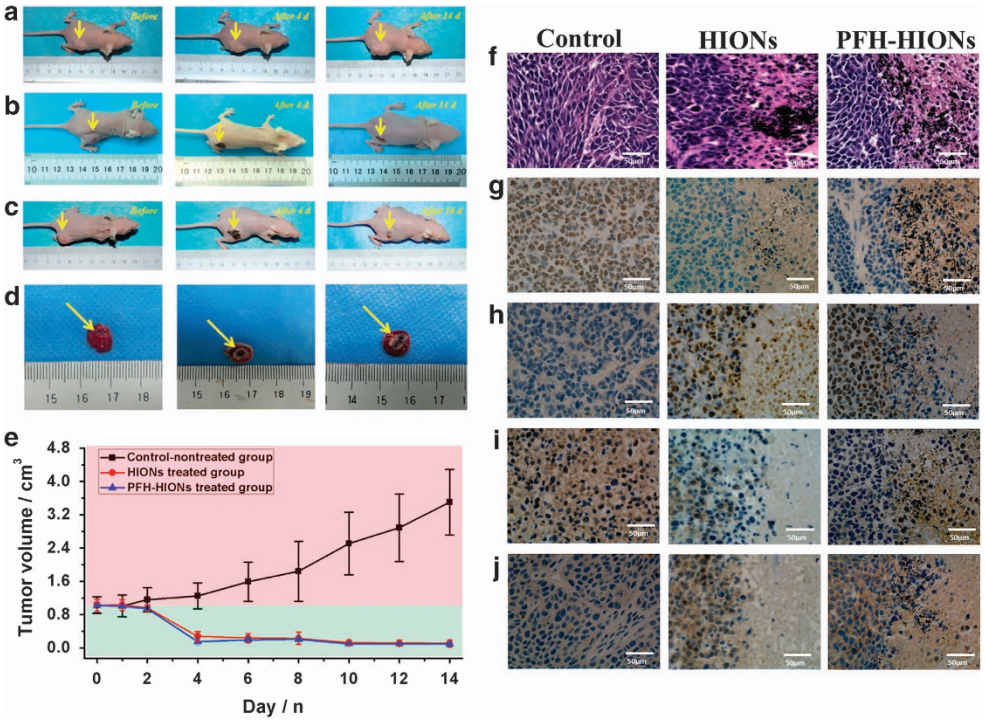

Figure 6 *In vivo* magnetic hyperthermia of tumor assisted by the performance of perfluorohexane-hollow iron oxide nanoparticles (PFH-HIONs). Photographs of tumors after the administration of (**a**) saline, (**b**) HIONs and (**c**) PFH-HIONs, and subsequent magnetic hyperthermia for 3 min. The images were recorded before and after the treatments for 4 and 14 days. (**d**) Photographs of tumors obtained by surgical removal after the administration of saline (left image), HIONs (middle image) and PFH-HIONs (right image) and subsequent magnetic thermal ablation. (**e**) Tumor growth curve of volume after the treatment of saline as the control, HIONs and PFH-HIONs as the therapeutic group, and further magnetic hyperthermia. (**f**) H&E staining and (**g**–**j**) optical microscopic images of immunohistochemical staining of tumor slices after the treatment by saline, HIONs and PFH-HIONs, and further magnetic hyperthermia. (**g**: PCNA, **h**: TUNEL, **i**: Bcl-2 and **j**: caspases).

an intelligent cancer treatment modality should release drug on-demand, improve diagnostic imaging or synergistic therapy. A new concept of MDV using a.c. magnetic field as the triggering source for cancer theranostics can effectively overcome the drawbacks of traditional ADV and ODV because there is no gas/bone influence of ultrasound or penetration depth limitations of a laser.[18–20,44,45] The stimuli-responsive vaporization process to produce microbubbles can substantially enhance ultrasound imaging, which can be further used for ultrasonography-guided magnetic hyperthermia of cancer. Importantly, the trigger by the a.c. magnetic field does not damage normal tissues where only small amount of PFH-HIONs are present. A small amount of PFH-HIONs was not heated by the a.c. magnetic field, as demonstrated by *in vitro* evaluations (Supplementary Figure S6).This unique MDV process can also solve the critical issues of particle size limitations of CAs for ultrasonography. In addition, the adopted superparamagnetic HIONs can act as the CAs for efficient *in vitro* (Supplementary Figure S13) and *in vivo* (Supplementary Figure S14) T_2-weighted magnetic resonance imaging, which leaves the potential for pre-determination of tumor tissues for the subsequent magnetic hyperthermia. It is noted that PFH-HIONs can penetrate the tumor vascular endothelial gap and diffuse into the tumor as demonstrated by the Prussian blue staining of tumor tissue after intravenous administration of PFH-HIONs into tumor-bearing mice (Supplementary Figure S15). Importantly, the composition of PFH-loaded HIONs was biocompatible because each component, PFH and HIONs, was highly biocompatible and has been extensively used in biomedical applications. Therefore, it was believed that the integration of PFH and HIONs maintained the biocompatibility feature, which was further demonstrated by an *in vitro* cytotoxicity test (Supplementary Figure S16), H&E staining (Supplementary Figure S17) of the main organs (heat, liver, spleen, lung and kidney) and a serum biochemical level evaluation (Supplementary Figure S18) after the magnetic hyperthermia where no obvious pathological changes were observed. Finally, the PFH-HIONs could be excreted out of the body as demonstrated by the Prussian blue staining of the main organs after magnetic hyperthermia treatment (Supplementary Figure S19).

CONCLUSIONS

In summary, we have developed a new concept of MDV for efficient stimuli-responsive cancer theranostics. The specific MDV process uses a.c. magnetic field as the artificially introduced trigger can efficiently solve the critical issues and limitations of traditional ADV and MDV processes. During the MDV process, superparamagnetic HIONs loaded with PFH can efficiently respond to a.c. magnetic field to raise the tumor temperature, which can vaporize the encapsulated PFH to substantially enhance the ultrasonography performance, as demonstrated both *in vitro* and *in vivo*. Importantly, the MDV process can also efficiently ablate the tumor tissues to completely remove the tumor. Because of the versatility of this unique MDV process, this new strategy can find broader applications in cancer theranostics compared with traditional ADV and ODV processes.

CONFLICT OF INTEREST

The authors declare no conflict of interest.

ACKNOWLEDGEMENTS

We acknowledge the financial support from the 973 program (No. 2014CB744500), the National Science Foundation for Distinguished

Young Scholars (81425014), the National Nature Science Foundation of China (No. 81227801, 81130025, 81270021, 81401433 and 81271598), the Chongqing Fund for Distinguished Young Scholars (cstc2013jcyjjq10004) and the Program for New Century Excellent Talent in University (NCET-13-1067).

1 Wagner, V., Dullaart, A., Bock, A. K. & Zweck, A. The emerging nanomedicine landscape. *Nat. Biotechnol.* **24**, 1211–1217 (2006).
2 Piao, Y., Kim, J., Na, H. B., Kim, D., Baek, J.S., Ko, M.K., Lee, J. H., Shokouhimehr, M. & Hyeon, T. Wrap-bake-peel process for nanostructural transformation from beta-FeOOH nanorods to biocompatible iron oxide nanocapsules. *Nat. Mater.* **7**, 242–247 (2008).
3 Medarova, Z., Pham, W., Farrar, C., Petkova, V. & Moore, A. *In vivo* imaging of siRNA delivery and silencing in tumors. *Nat. Med.* **13**, 372–377 (2007).
4 Peer, D., Karp, J. M., Hong, S., Farokhzad, O. C., Margalit, R. & Langer, R. Nanocarriers as an emerging platform for cancer therapy. *Nat. Nanotechnol.* **2**, 751–760 (2007).
5 Allen, T. M. & Cullis, P. R. Drug delivery systems: entering the mainstream. *Science* **303**, 1818–1822 (2004).
6 Chen, Y., Chen, H. & Shi, J. *In vivo* bio-safety evaluations and diagnostic/therapeutic applications of chemically designed mesoporous silica nanoparticles. *Adv. Mater.* **25**, 3144–3176 (2013).
7 Ferrari, M. Cancer nanotechnology: opportunities and challenges. *Nat. Rev. Cancer* **5**, 161–171 (2005).
8 Chen, Y., Chen, H. & Shi, J. Inorganic nanoparticle-based drug codelivery nanosystems to overcome the multidrug resistance of cancer cells. *Mol. Pharm.* **11**, 2495–2510 (2013).
9 Lee, N., Choi, S. H., Hyeon, T. & Nano-Sized, CT Contrast agents. *Adv. Mater.* **25**, 2641–2660 (2013).
10 Lee, J. E., Lee, N., Kim, T., Kim, J. & Hyeon, T. Multifunctional mesoporous silica nanocomposite nanoparticles for theranostic applications. *Acc. Chem. Res.* **44**, 893–902 (2011).
11 Na, H. B., Song, I. C. & Hyeon, T. Inorganic nanoparticles for MRI contrast agents. *Adv. Mater.* **21**, 2133–2148 (2009).
12 Lee, N. & Hyeon, T. Designed synthesis of uniformly sized iron oxide nanoparticles for efficient magnetic resonance imaging contrast agents. *Chem. Soc. Rev.* **41**, 2575–2589 (2012).
13 Kang, E., Min, H. S., Lee, J., Han, M.H., Ahn, H. J., Yoon, I. C., Choi, K., Kim, K., Park, K. & Kwon, I. C. Nanobubbles from gas-generating polymeric nanoparticles: ultrasound imaging of living subjects. *Angew. Chem. Int. Ed.* **49**, 524–528 (2010).
14 Schutt, E. G., Klein, D. H., Mattrey, R. M. & Riess, J. G. Injectable microbubbles as contrast agents for diagnostic ultrasound imaging: the key role of perfluorochemicals. *Angew. Chem. Int. Ed.* **42**, 3218–3235 (2003).
15 Chen, Y., Chen, H. & Shi, J. Nanobiotechnology promotes noninvasive high-intensity focused ultrasound cancer surgery. *Adv. Healtc. Mater.* **4**, 158–165 (2015).
16 Zhou, Y., Wang, Z., Chen, Y., Shen, H., Luo, Z., Li, A., Wang, Q., Ran, H., Li, P., Song, W., Yang, Z., Chen, H., Wang, Z., Lu, G. & Zheng, Y. Microbubbles from gas-generating perfluorohexane nanoemulsions for targeted temperature-sensitive ultrasonography and synergistic HIFU ablation of tumors. *Adv. Mater.* **25**, 4123–4130 (2013).
17 Wang, X., Chen, H., Zheng, Y., Ma, M., Chen, Y., Zhang, K., Zeng, D. & Shi, J. Au-nanoparticle coated mesoporous silica nanocapsule-based multifunctional platform for ultrasound mediated imaging, cytoclasis and tumor ablation. *Biomaterials* **34**, 2057–2068 (2013).
18 Shpak, O., Verweij, M., Vos, H. J., de Jong, N., Lohse, D. & Versluis, M. Acoustic droplet vaporization is initiated by superharmonic focusing. *Proc. Natl Acad. Sci. USA* **111**, 1697–1702 (2014).
19 Kagan, D., Benchimol, M.J., Claussen, J.C., Chuluun-Erdene, E., Esener, S. & Wang, J. Acoustic droplet vaporization and propulsion of perfluorocarbon-loaded microbullets for targeted tissue penetration and deformation. *Angew. Chem. Int. Ed.* **51**, 7519–7522 (2012).
20 Kang, S.-T. & Yeh, C.-K. Intracellular acoustic droplet vaporization in a single peritoneal macrophage for drug delivery applications. *Langmuir* **27**, 13183–13188 (2011).
21 Strohm, E., Rui, M., Gorelikov, I., Matsuura, N. & Kolios, M. Vaporization of perfluorocarbon droplets using optical irradiation. *Biomed. Opt. Express* **2**, 1432–1442 (2011).
22 Jian, J., Liu, C., Gong, Y., Su, L., Zhang, B., Wang, Z., Wang, D., Zhou, Y., Xu, F., Li, P., Zheng, Y., Song, L. & Zhou, X. India ink incorporated multifunctional phase-transition nanodroplets for photoacoustic/ultrasound dual-modality imaging and photoacoustic effect based tumor therapy. *Theranostics* **4**, 1026–1038 (2014).
23 Sun, Y., Wang, Y., Niu, C., Strohm, E. M., Zheng, Y., Ran, H., Huang, R., Zhou, D., Gong, Y., Wang, Z., Wang, D. & Michael, C. K. Laser-activatible PLGA microparticles for image-guided cancer therapy *in vivo*. *Adv. Funct. Mater.* **24**, 7674–7680 (2014).
24 Lee, J. H., Jang, J. T., Choi, J. S, Moo, S. H., Noh, S. H., Kim, J. W., Kim, J. G., Kim, I.S., Park, K.I. & Cheon, J. Exchange-coupled magnetic nanoparticles for efficient heat induction. *Nat. Nanotechnol.* **6**, 418–422 (2011).
25 Chen, Y., Jiang, L., Wang, R., Lu, M., Zhang, Q., Zhou, Y., Wang, Z., Lu, G., Liang, P., Ran, H., Chen, H. & Zheng, Y. Injectable smart phase-transformation implants for highly efficient *in vivo* magnetic-hyperthermia regression of tumors. *Adv. Mater.* **26**, 7468–7473 (2104).
26 Chen, Y., Chen, H., Sun, Y., Zheng, Y., Zeng, D, Li, F., Zhang, S., Wang, X., Zhang, K., Ma, M., He, Q., Zhang, L. & Shi, J. Multifunctional mesoporous composite nanocapsules for highly efficient MRI-guided high-intensity focused ultrasound cancer surgery. *Angew. Chem. Int. Ed.* **50**, 12505–12509 (2011).
27 Sun, Y., Zheng, Y., Ran, H., Zhou, Y., Shen, H., Chen, Y., Chen, H., Krupka, T. M., Li, A., Li, P., Wang, Z. & Wang, Z. Superparamagnetic PLGA-iron oxide microcapsules for dual-modality US/MR imaging and high intensity focused US breast cancer ablation. *Biomaterials* **33**, 5854–5864 (2012).
28 Gao, Z., Kennedy, A. M., Christensen, D. A. & Rapoport, N. Y. Drug-loaded nano/microbubbles for combining ultrasonography and targeted chemotherapy. *Ultrasonics* **48**, 260–270 (2008).
29 Rapoport, N. Y., Efros, A. L., Christensen, D. A., Kennedy, A. M. & Nam, K. H. Microbubble generation in phase-shift nanoemulsions used as anticancer drug carriers. *Bubble Sci. Eng. Technol.* **1**, 31–39 (2009).
30 Oeffinger, B. E. & Wheatley, M. A. Development and characterization of a nano-scale contrast agent. *Ultrasonics* **42**, 343–347 (2004).
31 Luo, B, Xu, S., Ma, W., Wang, W., Wang, S., Guo, J., Yang, W., Hu, J. & Wang, C. Fabrication of magnetite hollow porous nanocrystal shells as a drug carrier for paclitaxel. *J. Mater. Chem.* **20**, 7107–7113 (2010).
32 Wang, X., Chen, H., Chen, Y., Ma, M., Zhang, K., Li, F., Zheng, Y., Zeng, D., Wang, Q. & Shi, J. Perfluorohexane-encapsulated mesoporous silica nanocapsules as enhancement agents for highly efficient high intensity focused ultrasound (HIFU). *Adv. Mater.* **24**, 785–791 (2012).
33 Wang, Y., Shim, M. S., Levinson, N. S., Sung, H.-W. & Xia, Y. Stimuli-responsive materials for controlled release of theranostic agents. *Adv. Funct. Mater.* **24**, 4206–4220 (2014).
34 Chen, Y., Ye, D., Wu, M., Chen, H., Zhang, L., Shi, J. & Wang, L. Break-up of two-dimensional MnO2 nanosheets promotes ultrasensitive pH-triggered theranostics of cancer. *Adv. Mater.* **26**, 7019–7026 (2014).
35 Chen, Y., Meng, Q., Wu, M., Wang, S., Xu, P., Chen, H., Li, Y., Zhang, L., Wang, L. & Shi, J. Hollow mesoporous organosilica nanoparticles: a generic intelligent framework-hybridization approach for biomedicine. *J. Am. Chem. Soc.* **136**, 16326–16334 (2014).
36 Patel, K., Angelos, S., Dichtel, W. R., Coskun, A., Yang, Y. W., Zink, J. I. & Stoddart, J. F. Enzyme-responsive snap-top covered silica nanocontainers. *J. Am. Chem. Soc.* **130**, 2382–2383 (2008).
37 Liu, T., Wang, C., Gu, X., Gong, H., Cheng, L., Shi, X., Feng, L., Sun, B. & Liu, Z. Drug delivery with PEGylated MoS_2 nano-sheets for combined photothermal and chemotherapy of cancer. *Adv. Mater.* **26**, 3433–3440 (2014).
38 Ma., M., Xu, H., Chen, H., Jia, X., Zhang, K., Wang, Q., Zheng, S., Wu, R., Yao, M., Cai, X., Li, F. & Shi, J. A drug–perfluorocarbon nanoemulsion with an ultrathin silica coating for the synergistic effect of chemotherapy and ablation by high-intensity focused ultrasound. *Adv. Mater.* **26**, 7378–7385 (2014).
39 Yu, J., Ju, Y., Zhao, L., Chu, X., Yang, W., Tian, Y., Sheng, F., Lin, J., Liu, F., Dong, Y. & Hou, Y. Multistimuli-regulated photochemothermal cancer therapy remotely controlled via Fe5C2 nanoparticles. *ACS Nano* **10**, 159–169 (2015).
40 Shin, J., Anisur, R. M., Ko, M. K., Im, G. H., Lee, J. H. & Lee, I. S. Hollow manganese phosphate nanoparticles as smart multifunctional probes for cancer cell targeted magnetic resonance imaging and drug delivery. *Nano Res.* **5**, 679–694 (2012).
41 Yang, C., Wu, J. & Hou, Y. Fe_3O_4 nanostructures: synthesis, growth mechanism, properties and applications. *Chem. Commun.* **47**, 5130–5141 (2011).
42 Yu, J., Chu, X. & Hou, Y. Stimuli-responsive cancer therapy based on nanoparticles. *Chem. Commun.* **50**, 11614–11630 (2014).
43 Yu, J,. Yang, C., Li, J., Ding, Y., Zhang, L., Yousaf, M. Z., Lin, J., Pang, R., Wei, L., Xu, L., Sheng, F., Li, C., Li, G., Zhao, L. & Hou, Y. Multifunctional Fe5C2 nanoparticles: a targeted theranostic platform for magnetic resonance imaging and photoacoustic tomography-guided photothermal therapy. *Adv. Mater.* **26**, 4114–4120 (2014).
44 Fabiilli, M. L., Lee, J. A., Kripfgans, O. D., Carson, P. L. & Fowlkes, J. B. Delivery of water-soluble drugs using acoustically triggered perfluorocarbon double emulsions. *Pharm. Res.* **27**, 2753–2765 (2010).
45 Zhang, M., Fabiilli, M., Carson, P., Padilla, F., Swanson, S., Kripfgans, O. & Fowlkes, B. Acoustic droplet vaporization for enhancement of thermal ablation by high intensity focused ultrasound. *Acad. Radiol.* **18**, 1123–1132 (2011).

Supplementary Information accompanies the paper on the NPG Asia Materials website (http://www.nature.com/am)